

# 1 **Strain within mass-transport complexes (MTCs): seismic** 2 **characterisation and structural restoration, offshore** 3 **Uruguay** 4

5 Michael J. Steventon<sup>1\*</sup>, Christopher A-L. Jackson<sup>1</sup>, David M. Hodgson<sup>2</sup> & Howard D. Johnson<sup>1</sup>

6  
7 <sup>1</sup>Basins Research Group, Department of Earth Science & Engineering, Imperial College, Prince Consort  
8 Road, London, SW7 2BP, UK

9 <sup>2</sup>School of Earth and Environment, University of Leeds, Leeds, LS2 9JT, UK

10 \*Corresponding author: [michael.steventon13@imperial.ac.uk](mailto:michael.steventon13@imperial.ac.uk)

11  
12 7029 words (excluding references (2135) & figure captions (538)).  
13

## 14 **ABSTRACT**

15 Strain style, magnitude, and distribution within mass-transport complexes (MTCs) is important for  
16 understanding the process evolution of mass flows on continental margins and estimating their runout  
17 distances. Structural restoration and quantification of strain in gravitationally-driven margins have been  
18 shown to approximately balance, but this has not been attempted previously for an MTC. Hence,  
19 quantifying and characterising internal structural and stratigraphic variability within MTCs will help  
20 develop our understanding of strain distribution. We interpret and structurally restore a shallowly buried  
21 (c. 1500 mbsf) and well-imaged MTC, offshore Uruguay using a high-resolution (12.5 m vertical and  
22 15x12.5 m horizontal resolution) 3D seismic-reflection survey. This allows us to characterise and  
23 quantify vertical and lateral strain distribution within the MTC. Detailed seismic mapping and attribute  
24 analysis shows that the MTC is characterised by a complicated array of kinematic indicators, which  
25 vary spatially in style and concentration. Seismic-attribute extractions reveal several previously  
26 undocumented fabrics preserved in the MTC (e.g. sub-orthogonal shear zones), which suggest multiple  
27 phases of flow and transport directions during emplacement. The MTC is characterised by a broadly  
28 tripartite strain distribution, with extensional (e.g. normal faults), translational and compressional (e.g.  
29 folds and thrusts) domains, along with a radial frontally emergent zone. Inclusion of the frontally  
30 emergent zone is important for (1) producing balanced sections in restoration calculations, and (2)  
31 estimating compressional strain, which can cause a reduction of up to 8%. Results reveal how strain is  
32 preferentially concentrated around major structures (e.g. rafted-blocks), and quantifies the strain  
33 expressed on a seismic-scale within the extensional and compressional domains. Overall, we observed  
34 a strain deficit between the extensional and compressional domains (c. 3-14%), which is attributed to a  
35 combination of variables, including distributed (i.e. sub-seismic) strain, de-watering and sediment  
36 volume changes. This work has implications for assessing MTCs strain distribution and provides a  
37 practical approach for evaluating structural interpretations.  
38

39 *Keywords: mass-transport deposit, submarine landslide, Punta del Este, Oriental del Plata, kinematic*  
40 *indicators, seismic geomorphology, deep-water depositional systems*

## 41 1. INTRODUCTION

42 Mass-transport complexes (MTCs) are gravity-driven shear failure deposits resulting from creep, slide,  
43 slump, and debris flow processes (e.g. Dott 1963; Nardin 1979; Nemeč 1990; Weimer 1990;  
44 Posamentier & Martinsen 2011). Estimation of strain distribution within MTCs is important for  
45 understanding the deformation of partially lithified sediment on continental margins. Numerous studies  
46 have demonstrated the key role that MTCs play in (1) continental margin construction, (2) petroleum  
47 systems development, and (3) geohazard prediction (e.g. Posamentier & Kolla 2003; Weimer & Shipp  
48 2004; Moscardelli et al. 2006; Armitage & Stright 2010; Meckel 2011; Clare et al. 2017). The structures  
49 and kinematic indicators present within MTCs have been well documented by many seismic-reflection  
50 and outcrop-based works (e.g. Prior et al. 1984; Masson et al. 1993; Frey-Martínez et al. 2006; Gee et  
51 al. 2006; Bull et al. 2009; Ortiz-Karpf et al. 2016; Sobiesiak et al. 2017; Alsop et al. 2018). Yet,  
52 understanding strain distribution within MTCs has been limited by data type and quality: outcrop studies  
53 lack continuous observations from the extensional to compressional domain (Martinsen & Bakken  
54 1990), and seismic data is limited by a lack of internal bedding preservation, imaging quality and data  
55 resolution (e.g. Frey-Martínez et al. 2006). A systematic characterisation and quantitative restoration of  
56 intra-MTC strain thus requires relatively high-resolution 3D seismic-reflection data that image the full  
57 extent of a large MTC.

58 In contrast, structural restoration and quantification of strain on very large gravitational margins is  
59 common (i.e. up to 500 km in dip extent; up to 6 km thick). These systems typically develop on shale  
60 or salt detachments (e.g. Hudec & Jackson 2004; Butler & Paton 2010) and demonstrate that up-dip  
61 extension, typically accommodated by normal faulting, is broadly balanced downdip by folding and  
62 thrusting (Rowan et al. 2004). Similarly, in MTCs it may be suggested that upslope extension is  
63 approximately balanced by downslope contraction (e.g. Farrell 1984; Martinsen & Bakken 1990).  
64 However, despite MTCs containing a similar overall morphology to larger gravitational margins,  
65 previous studies have been unable to quantify strain distribution across an entire MTC, mainly due to  
66 data limitations.

67 Hence, this study aims to interpret and structurally restore a well-imaged, shallowly buried MTC (c.  
68 1500 mbsf) using a high-resolution 3D seismic-reflection survey. The dataset straddles the inshore  
69 Punta del Este and deep-water Oriental del Plata basins, offshore Uruguay (Fig. 1). The seismic-  
70 interpretation provides a framework for constructing a 2D structural restoration model and quantifying  
71 the lateral strain. The specific objectives are as follows: (1) assess intra-MTC strain distribution, (2)  
72 quantify extensional and compressional strain through palinspastic restoration, (3) test the hypothesis  
73 that MTC strain is best defined by a broadly tripartite strain distribution, (4) characterise vertical and  
74 longitudinal strain distributions within the MTC, (5) investigate how strain is partitioned around major  
75 structures within and beneath the MTC. Our approach will aid in detailed extraction of MTCs structural  
76 complexities and support the assessment of seal integrity of MTCs

77

## 78 2. GEOLOGICAL SETTING

79 Sedimentary basins offshore Uruguay form part of the Gondwanan break-up cycle and subsequent  
80 northward propagation of South Atlantic opening during the Late Jurassic-Early Cretaceous  
81 (Rabinowitz & LaBrecque 1979; Nürnberg & Müller 1991) (Fig. 1). Rifting occurred in two main  
82 phases: (i) an initial Jurassic phase that failed to produce oceanic crust, and which resulted in the  
83 formation of a NW-trending rift that is recorded in the nearshore Punta del Este and Argentine basins;  
84 and (ii) a second, Early Cretaceous phase, which is recorded in the distal Punta del Este, Pelotas and  
85 Brazilian basins, where it is related to formation of a NE-trending rift (Soto et al. 2011).

86 Four main sedimentary megasequences are identified offshore Uruguay: (i) a Paleozoic pre-rift  
87 sequence, (ii) a Jurassic-Early Cretaceous syn-rift sequence, (iii) a Barremian-Aptian transition

88 sequence, and (iv) a Aptian-Holocene post-rift sequence (Morales et al. 2017). This study focuses on  
89 the up to 3 km thick, Neogene to Holocene post-rift sequence. In the Punta del Este basin, Neogene to  
90 Holocene deposition occurred in association with overall progradation of large (up to 1.5 km tall)  
91 clinoforms. The MTC studied here occurs downdip of these clinoforms, above a regional Miocene  
92 unconformity (Conti et al. 2017) (Fig. 2).

93

### 94 **3. DATASET & METHODS**

#### 95 *3.1. Dataset and seismic interpretation*

96 The 3D pre-stack depth migrated (PSDM) seismic reflection survey used in this study covers an area of  
97 *c.* 13,000 km<sup>2</sup>. The data are SEG reverse polarity standard (European polarity, i.e. an increase in acoustic  
98 impedance = trough), have a stacking bin spacing of 15×12.5 m and a vertical resolution (limit of  
99 separability) of *c.* 12.5 m at 2.5 km depth. A shallowly buried, and thus seismically well-imaged, MTC  
100 was selected for detailed analysis and structural restoration (Fig. 1). We mapped the base and top of the  
101 MTC, in addition to numerous internal faults and several internal reflections. Mapping enabled  
102 construction of isopach maps, extraction of kinematic indicators and calculation of MTC strain. No  
103 wells penetrate through the MTC thus we cannot constrain the lithology or precise age of emplacement.

104

#### 105 *3.2. Seismic attribute analysis*

106 Several geometric-, amplitude-, and frequency-based attributes were used to assess the external and  
107 internal morphology of the MTC. Seismic variance (coherency) was calculated based on the Van  
108 Bemmél & Pepper (2000) edge detection method, allowing better imaging and mapping of  
109 discontinuities, such as intra-MTC faults. Seismic attributes are often sensitive to noise within the input  
110 data (REF). Hence, the raw reflectivity data was conditioned by a single layer-parallel smoothing  
111 iteration before variance attribute computation. We also used ant-tracking, a method of enhancing  
112 discontinuities in 3D seismic data, to image and map fault/fracture networks (Randen 1998; Randen et  
113 al. 2001). We also applied spectral decomposition to the raw reflectivity data; this splits the seismic  
114 signal into narrow frequency bins (i.e. low, mid and high) that, when blended together, highlight  
115 structural and stratigraphic heterogeneities (see Partyka et al. 1999). Several grid-based attributes, such  
116 as dip magnitude and root-mean squared (RMS) amplitude, were also employed to aid interpretations.  
117 In addition to grid-based surface attribute extractions, we also undertook iso-proportional slicing within  
118 the MTC to capture internal structural fabrics. This method is similar to techniques used for detailed  
119 reservoir delineation studies that provide an extra level of detail (see Zeng et al. 1998).

120

#### 121 *3.3. Decompaction and structural restoration*

122 A kinematic restoration of the MTC was undertaken to assess longitudinal (i.e. sediment transport-  
123 parallel) strain. Restoration was used to test the validity of the seismic interpretation (i.e. does the  
124 section balance and preserve rock volume, thickness, length, etc.) and to quantify strain distribution  
125 within the MTC (Dahlstrom 1969; Hossack 1979; Lingrey & Vidal-Royo 2015). We assume only plane-  
126 strain deformation (i.e. extension and shortening parallel to the bulk sediment transportation direction)  
127 and preservation of line-length. However, out-of-plane strain, in addition to volume loss due to vertical  
128 transport (re-suspension) of material out-of-section could occur. To help mitigate these effects, we  
129 orientated the restored sections parallel to the dominant MTC transport direction through analysis of  
130 kinematic indicators such as lateral margins (Fig. 3A). Due to the component of ductile strain within  
131 MTCs, simple shear and flexural slip methods have also been tested and compared with the line-length  
132 approach to quantify model sensitivities (Lingrey & Vidal-Royo 2015).

133 Before calculating longitudinal strain, the MTC was decompacted to remove the effects of volume  
 134 decrease driven by burial-related porosity reduction. Constraining pre-compaction thickness, and thus  
 135 immediately post-emplacement structural geometries of intra-MTC faults and folds, allows a more  
 136 accurate calculation of corrected strain magnitudes. Backstripping of the overburden was undertaken  
 137 on a layer-by-layer basis (three layers in total). As input to the decompaction process we assumed initial  
 138 surface porosities of 0.63 and 0.49, and rates of porosity decay of 0.51 and 0.27  $\text{Km}^{-1}$  for shale and  
 139 sandstone. This is based on the Sclater & Christie (1980) decompaction curve ( $\phi = \phi_0(e^{-cz})$ ), where  
 140  $\phi/\phi_0$  relates to present-day and surface porosities, respectively. The MTC-dominated overburden is  
 141 assumed to have the same lithological characteristics as the studied, more deeply buried MTC (Fig. 4-  
 142 A). The composition of the MTC (45% clay, 45% silt, 10% sand) was estimated from a shallow core  
 143 sample (GeoB13860-1) taken from a seafloor MTC on the Uruguayan margin (Krastel et al. 2011). This  
 144 lithological composition is comparable to MTCs observed at outcrop (e.g. Pickering & Corregidor  
 145 2005), although MTCs are, by their nature, compositionally highly variable.

146 The strain ( $e$ ) of folded and faulted pre-kinematic strata can be approximated by summing the individual  
 147 segments of a horizon ( $L_0 = H_1 + H_n$ ) and comparing this to the present length ( $L_1$ ) (1). The calculated  
 148 strain is at best a minimum estimate, as only macro-scale structures are identifiable and thus restorable  
 149 (i.e. sub-seismic faulting and folding cannot be explicitly accounted for using this method; e.g. Marrett  
 150 & Allmendinger (1992). Thus, an mismatch in balancing of between 2-60% may be ascribed to variables  
 151 that cannot be identified using seismic data; we discuss later potential ways in which we can mitigate  
 152 these uncertainties (Marrett & Allmendinger 1992; Burberry 2015). Structural restoration also carries  
 153 interpretation errors, with our interpretation of structures being subjective and non-unique, and likely  
 154 biased towards our previous geological experiences and concepts. Variations in interpretation of fault-  
 155 horizon cut-offs may also produce bed length errors of up to  $\pm 10\%$  (Judge & Allmendinger 2011).

156

$$157 \quad e = (L_1 - L_0)/L_0 \quad (1)$$

158

159 MTCs are typically defined by packages of chaotic reflections (e.g. Posamentier & Kolla 2003). The  
 160 MTC studied here is no exception, thus it was not possible to interpret internal reflections across the  
 161 entire deposit. Hence, 2D rather than 3D restoration techniques were used.

162

## 163 4. SEISMIC CHARACTERISATION OF THE MTC

### 164 4.1. General characteristics and nature of bounding surfaces

165 The studied MTC comprises low-amplitude, chaotic seismic reflections, with a high-amplitude, semi-  
 166 continuous basal reflection that caps a polygonally-faulted mudstone sequence (Fig. 4). The high-  
 167 amplitude basal reflection is interpreted as a basal shear surface, representing a *kinematic boundary*  
 168 *layer* (sensu Butler et al. 2016) or zone, upon which the MTC was translated (Varnes 1978; Martinsen  
 169 1994). The basal shear surface connects updip to a headwall scarp and downdip to a frontal ramp, which  
 170 define the limit of the extensional and compressional domains, respectively. Across the majority of the  
 171 MTC, the basal shear surface is laterally continuous and concordant with underlying stratigraphy,  
 172 except for where it cuts up through stratigraphy at the lateral margin. Locally, however, there is  
 173 considerable relief (up to 460 m) along the basal shear surface in the form of steps and ramps (sensu  
 174 Bull et al. 2009). Elsewhere, more subtle steps and ramps (upto 75 m relief) cut into the underlying  
 175 substrate.

176 The top of the MTC is hummocky (vertical relief 13-65 m) and of highly variable reflectivity (Fig. 4).  
 177 In areas undisrupted by later deposition, the top surface is expressed as a positive reflection, defining a

178 downward decrease in acoustic impedance. Elsewhere, the reflection is either highly variable or  
179 undefinable with no discrete structural features (i.e. faulting or folding). Directly beneath the top surface  
180 there is a highly chaotic, weakly reflective zone, with no distinct structures visible (Fig. 4-C). The highly  
181 chaotic seismic facies can also be seen to infill topographic relief between fold-thrust structures and  
182 shear zones and rapidly thins within the frontally emergent zone. The chaotic seismic facies may  
183 represent a mud-rich debris flow (debrite), which formed during or after the MTC. We interpret the  
184 geometric irregularity and acoustic variability in the top surface reflects a combination of (1) scouring  
185 and incision of the MTC by later mass-flow events, (2) a component of high yield strength of the  
186 overlying debrite, and (3) the effect of large coherent blocks (Fig. 4-C & Fig. 6-A) (Hodgson et al.  
187 2017).

188 The MTC is thickest (upto 550 m) and has the greatest relief on the top surface along the eastern and  
189 western margins, where folding and thrusting is concentrated (Fig. 3). The MTC thins significantly to  
190 the east-southeast due to incision and erosion by later MTCs, which limits identification of the eastern  
191 margin (Fig. 3-B & Fig. 5-A). These margins outlining the eastern and western boundary of the MTC  
192 are interpreted as lateral margins, where layer-normal shear would have been orientated approximately  
193 parallel to the paleo-slope (Alsop & Holdsworth 2007; Debacker et al. 2009). The lateral margins are  
194 most prominent within the compressional domain and are linked to both the headwall scarp and frontal  
195 ramp. They are up to 300 m high separating the MTC from surrounding undisrupted deposits and  
196 indicate a translation direction towards the south-east (153-118°).

197 We recognise four internal domains within the studied MTC: (i) an extensional domain defined by a  
198 headwall scarp and normal faults, (ii) a chaotic translational domain, (iii) a compressional domain, and  
199 (iv) a frontally emergent zone (Fig. 4-A) (cf. Posamentier & Kolla 2003; Moscardelli et al. 2006;  
200 Lamarche et al. 2008; Bull et al. 2009; Gamboa & Alves 2016). We describe these domains below.

#### 201 4.2. Extensional domain

202 The headwall scarp bounds the updip extent of the extensional domain, being instantly recognisable in  
203 variance extraction maps as the boundary between the undeformed slope and the strongly deformed (i.e.  
204 seismically chaotic) MTC (Fig. 5-A). The headwall scarp trends NE-SW, approximately parallel to the  
205 paleo-slope and rather than having the characteristic arcuate shape (cf. Bull et al. 2009), is fragmented.  
206 Numerous NE-SW-striking (i.e. broadly scarp-parallel), gently (20-35°) SE-dipping normal faults occur  
207 immediately downdip of the scarp. Further downdip, towards the translational domain, these faults are  
208 smaller, and thus below seismic resolution, or are truly absent. An alternative interpretation is that the  
209 faults in this region are overprinted and reworked by the chaotic matrix fabric (Fig. 4-B). The  
210 extensional domain forms a relatively small section of the MTC, being 6.5-20 km in width.

#### 211 4.3. Translational domain

212 The length and character of the translational domain is highly variable along strike (Fig. 3-B and 4-C),  
213 being narrowest (<5 km) where the extensional and compressional domains almost merge, and widest  
214 (c.18 km) near the central part of the MTC, where large blocks of continuous, often high-amplitude  
215 reflections occur. Many of these blocks are deformed by normal faults, which may also deform the  
216 underlying basal shear surface (Fig. 6-A). The NNE-SSW strike of the moderately dipping (c. 35-50°)  
217 normal faults, suggests a SE-orientated minimum compressive stress ( $\sigma_3$ ) approximately parallel to the  
218 overall MTC transport direction. Small, arcuate fold-thrust systems occur below several of these blocks  
219 within the basal shear surface/zone (Fig. 6-A). At the base, variance and spectral decomposition  
220 extractions display the overall arcuate fold-thrust footprint, while the ant-track extractions reveal  
221 discontinuities relating to individual faults/fractures. The main mass of the block is clearly discernible  
222 as a coherent unit surrounded by a more chaotic matrix in the extractions at -150 m. At -300 m, the  
223 coherency of the block changes to fully opaque matrix facies (Fig. 6-A). This suggests the blocks were

224 transported, rather than representing remnant blocks (Jackson 2011; Gamboa & Alves 2015; Hodgson  
225 et al. 2017). The occurrence of compressional and extensional structures in the same area may suggest  
226 polyphase deformation and a strain sequence recording acceleration (i.e. normal) faulting and  
227 translation in the basal shear zone fold-thrust system.

#### 228 *4.4. Compressional and frontally emergent domains*

229 The compressional and frontally emergent domains characterise the downdip termination of the MTC  
230 (Frey-Martínez et al. 2006). In this example, the MTC climbs up the frontal ramp and becomes  
231 emergent, passing downdip into chaotic seismic reflections interpreted as a debrite. The compressional  
232 domain is highly deformed with a well-imaged fold-thrust system and shear zones

233 The fold-thrust system is the defining feature of the compressional domain (Figs. 4-D, 5-B, 5-D). In  
234 map view, the domain is radial, with the fold-thrust system trending 015°-195° in the east to 100°-280°  
235 in the west. The thrusts typically dip 30-40° (some up to >60°) towards the NW (i.e. updip).  
236 Displacements range from 12.5 (minimum vertical resolution) to 175 m and vary along strike, with  
237 relays (fault-linkage) forming between individual thrust segments (Fig. 6-B). The thrusts detach  
238 downwards onto the basal shear surface and can affect the entire vertical extent of the MTC, particularly  
239 towards the frontal ramp. The thrusts are flanked by and dissect hangingwall anticlines and footwall  
240 synclines. These folds are gentle-to-open, non-cylindrical, and verge downdip towards the frontal ramp  
241 (Fig. 6-B). Folds are more open above the thrust tips, and tighter where they have been dissected by  
242 their related thrust; we infer this geometry records an initial phase of fault-propagation folding and open  
243 fold formation that was superseded by thrust propagation and fold dissected.

244 Two sets of shear zones are recognised, trending longitudinally (c.130°-310°) and sub-orthogonally (c.  
245 050°-230°) to the slope (Fig. 5-B & Fig 5-D). The longitudinal shears are imaged on the top surface as  
246 narrow zones (100-150 m) infilled by chaotic seismic facies, interpreted as the overriding debrite. We  
247 infer these shear zones record the junction between segments of the MTC where differential transport  
248 velocities have produced strike-slip motions (Masson et al. 1993; Gee et al. 2005). The sub-orthogonal  
249 shears produced 'V'-shaped depressions within the MTC, with the associated zones dipping upslope to  
250 the NW (Fig. 6-B). These depressions are up to 600 m wide and spaced at 2-6 km intervals along the  
251 western margin of the MTC (Fig. 5-B). At the base of the sub-orthogonal shears, bedded segments are  
252 juxtaposed against one another, whereas the depressions are filled from above by chaotic seismic facies  
253 (debrite). These shears probably reflect differing flow velocities within the basinward translating MTC  
254 (Bull et al. 2009). More specifically, individual segments appear to have interacted with the lateral  
255 margin and frontal ramp at different times during MTC emplacement. This may have caused segments  
256 (I) to (III) (see inset map Fig. 5-B) to decelerate intermittently, producing a component of right-lateral  
257 (dextral) internal shearing. Therefore, in addition to layer-normal shear, we also interpret a component  
258 of oblique compression against the western lateral margin to account for the modified fold-thrust system  
259 (Strachan & Alsop 2006; Sharman et al. 2015).

260 Beyond the frontal ramp and in the distal reaches of the lateral ramps, the seismic character of the MTC  
261 changes abruptly, from well-defined, albeit folded and thrustured reflections, into only chaotic reflections.  
262 We relate this change to a modification in transport dynamics from a confined to an unconfined system,  
263 allowing the MTC and overriding debrite to spread-out over the paleo-seafloor (Frey-Martínez et al.  
264 2006; Armandita et al. 2015). This reduction in confinement was associated with increased  
265 disaggregation and deformation of bedding, hence the downdip transition to debrite. As well as  
266 unconfined flow over the frontal ramp, spill-over of the flow occurred where fold-thrusts curve towards  
267 the margin in an upslope direction (Fig. 6-C).

#### 268 *4.5. Classification and transport direction*

269 Based on its geometry and scale (c. 500-150 m thick, 50 km long, 2400 km<sup>2</sup>), the MTC is classified as  
270 a *frontally emergent* (Frey-Martínez et al. 2006), *attached* MTC (*sensu* Moscardelli & Wood 2015).  
271 Furthermore, the Moore & Sawyer (2016) flow factor measure, which is a proxy for relative mobility,  
272 suggests the MTC has a low-medium mobility based on the hummocky top surface, well developed  
273 fold-thrust belt, and longitudinal shear zones. This would suggest an approximate transportation and  
274 deformational process spanning slump-slide rather than full plastic flow (Posamentier & Martinsen  
275 2011).

276 We have shown that the MTC displays predictable albeit variable strain distributions, defined by a  
277 relatively narrow, updip extensional domain, a transitional domain of variable width, and a relatively  
278 wide, downdip compressional domain including frontal and some lateral emergence. We have used the  
279 associated kinematic indicators in combination with the regional basin setting to estimate the overall  
280 transport direction 118°-162°; i.e. broadly SE. This analysis informs where we select our dip-sections  
281 for structural restoration, which we describe in the following section (Fig. 3-A & Fig. 4).

282

## 283 5. STRUCTURAL RESTORATION

284 Structural restoration was undertaken on two dip-oriented sections positioned orthogonal to the  
285 transport direction and dominant fault strikes; as discussed above, our assumption of broadly plane  
286 strain should thus be valid (Fig. 4). The sections are positioned near the western margin (Section 1) and  
287 centre (Section 2) of the MTC and were chosen due to the high-quality seismic imaging within the  
288 compressional domain and the relatively completeness of preservation (i.e. no later erosion by MTCs  
289 or submarine channels) (Fig. 3). In principle, strain within the MTC should approximately balance (i.e.  
290 extension = contraction) if the system is kinematically self-contained.

### 291 5.1. Model set-up and decompaction

292 The geometric input model to the restoration is based directly on the seismic-scale geometry of the  
293 studied MTC, consisting of a 12-20 km wide extensional domain, a wide 20-30 km compressional  
294 domain, and a 1-2 km wide translational area lacking seismic-scale structures (Fig. 7). The input model  
295 consists of the basal shear surface, top surface, several intra-MTC surfaces, normal faults (updip), and  
296 thrusts (downdip). As there are no translational structures in Section 1 that could be measured, a  
297 boundary (denoted E/C) was used in the model to mark the estimated mid-point between the  
298 compressional and extensional domains. In Section 2 we focus solely on the compressional domain due  
299 to the poor-imaging and lack of clear structures within the extensional domain. Hence, for Section 2 we  
300 aimed to understand the depth dependency of strain in the compressional domain, rather than evaluating  
301 longitudinal balancing. Two definitions of the compressional domain were considered: (1)  $H_C$ , which  
302 includes the frontally emergent, debrite-dominated zone; and (2)  $H_{C-f}$ , which excludes this zone (Fig.  
303 7). This distinction enabled quantification of the effects frontal emergence and distal ramps have on  
304 section balancing (e.g. Hudec & Jackson 2004).

305 The decompacted sections show a similar overall morphology to that presently observed, with minor  
306 geometric variations amplifying the extensional domain features to the north-west where overburden is  
307 thickest. After decompaction, the MTC increased in cross-sectional area by 27% (14.5 km<sup>2</sup> to 18.2 km<sup>2</sup>)  
308 and 23% (19.4 km<sup>2</sup> to 24.5 km<sup>2</sup>) for Sections 1 and 2, respectively.

309

### 310 5.2 Results

311 The present length of the extensional domain in Section 1 is 13.9 km, whereas the restored length,  
312 depending on the method used, is 12.0-12.3 km, equating to 13-16% of extension (Table 1). For Section

313 1, a single intra-MTC reflection ( $H3_C$ ) was interpreted through the compressional domain; the present-  
314 day length of this reflection is 32.3 km, whereas the restored length is 39.1-39.8 km, equating to 17-  
315 19% of horizontal shortening (Table 1). When the frontally emergent zone ( $H3_{C-f}$ ) is excluded, the  
316 horizontal shortening increases to 25-26%. Section 1 thus approximately balances, with the mismatch  
317 between of 3-14% (i.e. shortening strain < extensional strain) being within the bounds of expected error  
318 ( $\pm 2-40\%$ ) (Burberry 2015). The discrepancy increases when the frontally emergent zone is excluded,  
319 which is expected as only the most highly strained-area of the section is restored.

320 For Section 2, two internal horizons were interpreted: a lower horizon,  $H3_{C_i}$ , and an upper horizon,  
321  $H3_{C_{ii}}$ . The present length of  $H3_{C_i}$  is 24.0 km, restoring to 31.8-32.8 km and thus yielding a horizontal  
322 shortening of 24-27%. When the frontally emergent zone ( $H3_{C_{ii}}$ ) is included in the restoration the  
323 horizontal shortening is 14-15%, increasing to 16-18% when this zone is excluded ( $H3_{C_{ii-f}}$ ). Although  
324 no observation can be made on the balancing of Section 2, vertical strain partitioning could be inferred  
325 between  $H3_{C_i}$  and  $H3_{C_{ii-f}}$ . The lower ( $H3_{C_i}$ ) has been shortened significantly more (24-27%) than the  
326 upper ( $H3_{C_{ii-f}}$ ) suggesting something intrinsic to the MTC that resulted in this apparent partitioning of  
327 strain.

328 Overall, the structural restoration of Section 1 provides some validity to the interpretation of the MTC.  
329 Nevertheless, the shortening is not fully balanced by extension. This suggests accommodation through  
330 other strain components, which cannot be accounted for using conventional structural restoration  
331 methods. Drawing comparisons with frontally emergent MTCs, including or excluding the frontally  
332 emergent zone in the restorations has significant implications for section balancing. Although no  
333 discrete macro-structures are visible in the zone it may be that sub-seismic structures are present and  
334 are accommodating extra strain. This can be demonstrated by comparing  $H3_{C_{ii}}$  to  $H3_{C_{ii-f}}$  (Table. 1),  
335 where strain in the frontally emergent zone accommodates c.13% of the total shortening experienced  
336 by the compressional domain. Inclusion of the frontally emergent zone in calculations of compression  
337 is significant; to produce an approximately balanced seismic-scale MTC (Table. 1) a certain percentage  
338 of shortening needs to be accommodated by this zone. Therefore, results that include the emergent zone  
339 are more realistic, even though a volume is partitioning away from the main MTC body it is still  
340 accommodating strain.

341

## 342 6. DISCUSSION

343 This section considers the MTC structure and emplacement mechanism, and discusses the advantages,  
344 limitations, and implications of the restoration approach for understanding intra-MTC strain.

345

### 346 6.1. Mode of MTC emplacement

347 The occurrence of radial spreading fold-thrust structures, the distribution of extensional-translational-  
348 compressional domains, the presence of stratified blocks and the relatively low degree of disaggregation  
349 suggest the MTC formed through slump-slide processes (e.g. Dott 1963; Nardin 1979; Merle 1989;  
350 Posamentier & Martinsen 2011).

351 The relationship between the MTC and its capping debrite may indicate: (1) the debrite is younger and  
352 thus genetically unrelated to, and simply fills relief created by the MTC, (2) the debrite and MTC are  
353 coeval, and/or (3) debrite deposition initiated *in-situ* failure of underlying sediments and formation of  
354 the MTC. The following observations support the latter interpretation: (1) thrust-related hangingwall  
355 anticlines in the distal domain are not eroded at the base of the capping debrite, (2) the close correlation  
356 between debrite thickness and MTC depressions (e.g. fold-troughs and shear zones), (3) rapid thinning  
357 of the debrite beyond the frontally emergent zone, and (4) no continuous erosional features such as

358 grooves or striations are observed at the base of the MTC suggesting a limited run-out distance (Figs 4-  
359 6).

360 Hence, deformation within the MTC was probably initiated by an overriding debris flow, which  
361 produces increased loading and localisation of shear stress on a mechanically weak zone (Fig. 8). This  
362 is consistent with similar observations from the field (e.g. Van der Merwe et al. 2009; Van Der Merwe  
363 et al. 2011) and from other seismic-based examples (e.g. Schnellmann et al. 2005; Watt et al. 2012),  
364 which all suggest shear coupling-type models. Initial triggering mechanisms for the debris flow are  
365 beyond the scope of this study. However, the basal shear surface of the MTC may have coincided with  
366 a low shear strength sediment layer produced by shallow gas. This is consistent with present-day signs  
367 of shallow gas, both below and above the MTC, in the form of a bottom-simulating reflector, bright  
368 spots and pockmarks (see supplementary material).

369

## 370 *6.2. Intra-MTC strain features*

371 We have demonstrated that seismic-scale structures in MTCs can be extracted using modern attribute  
372 techniques. This approach has allowed us to document two previously unrecognised types of intra-MTC  
373 structures using seismic-reflection data: (1) internal shearing in the form of sub-orthogonal shear zones,  
374 and (2) fold-thrust systems within the basal shear zone beneath rafted-blocks.

375 Longitudinal shear zones have been attributed to variations in MTC transport velocities (Masson et al.  
376 1993; Gee et al. 2005; Bull et al. 2009). The results from the MTC studied here suggests that  
377 emplacement was more complex than simple single-celled models suggest (see Farrell 1984). In  
378 addition to the more common longitudinal shear zones, there is a second sub-orthogonal set, which  
379 supports internal shearing linked to transport velocity variations, but this time oblique to the bulk  
380 sediment transport direction. This second set of shear zones seems to be intimately linked to the  
381 orientation of the western lateral margin (Fig. 5-B). Typically, lateral margins impose transtensional  
382 strain in areas of depletion (i.e. extensional domains) and transpressional strain in areas of volume  
383 increase (i.e. compressional domains) (Varnes 1978). Fleming & Johnson (1989) identified similar  
384 orientated ‘cracks’ along the lateral margins, when observing subaerial landslides in Utah, USA.  
385 However, to our knowledge, no such seismic-scale shear of this type has been documented. One  
386 interpretation may be that the sub-orthogonal shear zones record transpression within the compressional  
387 domain and could be classified as a form of riedal shear or extensional fracture. This provides evidence  
388 for a strike-slip/oblique slip component through the compressional domain of the MTC and shows that  
389 tri-partite strain distribution may be an oversimplification.

390 Another new observation is the development of minor fold-thrust systems beneath rafted blocks (Fig.  
391 6-A). Alves (2015) shows how large, rafted blocks may interact with basal shear surfaces, typically  
392 forming seismic-scale grooves (furrows) and scours. Field observations at the base of rafted blocks  
393 often show small-scale foliation and soft-sediment shear structures and, at a larger-scale, folding and  
394 injectites (Alves 2015; Hodgson et al. 2017). However, structures modifying the basal shear surface can  
395 be >100 m in height and extend across the aerial-footprint of a rafted-block recording the transportation  
396 pathway. Our observations support the notion of a basal shear zone of distributed strain, rather than  
397 distinct surface and correlates approximately with Alves & Lourenço (2010) block to basal shear zone  
398 thickness ratio (c. 0.2), approximately 0.22 for the block in Fig. 6-A. Our results suggest that previously  
399 observed rafted blocks in other 3D seismic-reflection case studies may also have modified the basal  
400 shear surface to create similar discrete structures (e.g. Hodgson et al. 2017). However, limitations to  
401 the spatial resolution of seismic-reflection data may, in the past, have prevented clear imaging of these  
402 structures. Furthermore, in the field there is a risk that the fold-thrust systems underneath rafted-blocks  
403 could be misinterpreted as compressional domains within smaller MTCs. Therefore, we suggest that

404 distributed strain in *attached*-MTCs is substantial enough to create upto 100 m thick zones of intense,  
405 predominantly contractional strain.

406 The identification of these intra-MTC structures demonstrates the way in which strain can be  
407 concentrated in discrete areas. This also illustrates why structural restoration results cannot be used in  
408 isolation to capture entire MTC strain characteristics. The detailed seismic attribute work presented  
409 here, including iso-proportional slicing, demonstrates the extra level of detail and spatial understanding  
410 of MTCs that is unparalleled, certainly when compared to isolated outcrops.

411

### 412 *6.3. Structural restoration and missing strain components*

413 Updip extensional and downdip compressional strain within the MTC approximately balance when  
414 including the frontally emergent zone. Compressional strain accommodates approximately 3 to 6%  
415 more strain, which is at least partly attributed to limitations of the restoration method. In addition, other  
416 aspects also have the potential to produce underestimated strain magnitudes and need to be considered  
417 further: (1) sub-seismic faults and folds, (2) volume loss due to lateral compaction, (3) porosity  
418 reduction and dewatering, and (4) strain overprinting

419

### 420 *Restoration techniques*

421 Variations in results between restoration methods line-length and flexural slip are insignificant in the  
422 compressional domain as both procedures preserve line length (Lingrey & Vidal-Royo 2015; Fossen  
423 2016). Simple shear shows a greater discrepancy with less compression between domains in Section 1,  
424 likely reflecting its inability to preserve line length and poor handling of steeper-dips. These results also  
425 show that definition of the lateral extent of the MTCs has a large impact on the compressional domain  
426 and, hence, whether or not a section can be balanced. Inclusion of the debrite-dominated material  
427 basinward of the frontal ramp is a key factor for MTC strain balancing. This suggests that a “foreland”  
428 type strain zone is apparent beyond the defined boundary of the MTC. Therefore, characterisation of  
429 the terminal emergent wedge of a frontally emergent MTC is critical for successful restoration.  
430 Otherwise, results may suggest insufficient compression.

431 There are several limitations imposed by palinspastic restoration and the line-length, flexural slip and  
432 simple shear methods. Line-lengths, and hence cross-sectional areas, are unlikely to be preserved in  
433 MTCs due to penetrative strain. For example, in order to understand deformation in the distal  
434 contractional domain, in particular the impact of so-called ‘cryptic’ lateral compaction may require the  
435 application of area sensitive methods, such as area-depth-strain (ADS) (e.g. Schlische et al. 2014).  
436 Additionally, physical and numerical models may allow more rigorous boundary conditions (e.g.  
437 porosity distributions) to be defined on the transformation of MTCs from semi-lithified sediments (e.g.  
438 Wang et al. 2017).

439

### 440 *Sub-seismic strain*

441 Despite the relatively high vertical and lateral resolution of our seismic-reflection dataset (12.5 by 12.5-  
442 15 m), not all intra-MTC structures can be imaged, most notably (1) discrete, albeit sub-seismic  
443 fractures and folds, and (2) more distributed, cryptic features associated with penetrative strain (e.g.  
444 intergranular deformation). Hence, the estimations of extension and compression represent minima  
445 values, since the restoration models only capture seismic-scale deformation. Although sub-seismic  
446 strain (penetrative strain) cannot be quantified in this MTC, there are numerous studies which have

447 attempted this (Kautz & Sclater 1988; Marrett & Allmendinger 1992; Walsh et al. 1996; Burberry 2015;  
448 Dalton et al. 2017)

449 Penetrative strain typically accommodates between 2-30% of overall shortening in horizontal  
450 shortening-related analogue models (Koyi et al. 2004; Burberry 2015). The amount of penetrative strain  
451 decreases away from thrust belts (Craddock & van der Pluijm 1989), with the magnitude of layer-  
452 parallel shortening increasing with depth (Koyi 1995). In physical models, the increase in shortening  
453 with depth (c.19%) is accommodated by (1) a decrease in bed-length, (2) an area-loss through lateral  
454 compaction in deeper layers, (3) layer-normal thickening of shallower layers, and (4) increased  
455 displacement on thrusts (Koyi 1995; Koyi et al. 2004; Groshong et al. 2012). We make similar  
456 observations in the up to 550 m thick MTC studied here, with strain increasing with depth from H3<sub>ii-f</sub>  
457 (18%) to H3<sub>i</sub> (27%), at least in Section 2. This suggests similar depth dependant layer-parallel  
458 shortening, perhaps related to one or a combination of the processes listed above. Physical models only  
459 record grain-grain displacement and, therefore, penetrative strain estimates are only considered a  
460 minima of that occurring in natural systems (Burberry 2015). The mechanisms of penetrative strain  
461 within the MTC are likely to include the following: (1) grain-grain displacements, (2) dewatering, minor  
462 folding and faulting, and (3) other minor structures only observable in the field (e.g. Sobiesiak et al.  
463 2017). Similar studies of high-porosity (40-70%) sediments at similar depths (i.e. 700 mbsf) experience  
464 horizontal ductile shortening of c. 12% before the formation of discrete structures (Henry et al. 2003).  
465 It is not possible to quantify the degree to which lateral porosity and fluid loss within the MTC without  
466 calibration from well data. However, we can assume that some component related to these mechanisms  
467 is being overlooked on a seismic-scale study. Therefore, we may expect penetrative strain in the  
468 compressional domain of the studied MTC to be larger than that estimated by physical models.

469 It is well known that seismic-reflection based restoration studies may underestimate true strain; for  
470 example, these data may underestimate 15-60% of the true extensional strain occurring in rift basins  
471 (Marrett & Allmendinger 1992; Walsh et al. 1996). This error is generally ascribed to seismic-resolution  
472 limitations, most notably (1) “small” fault populations, which contribute significant amounts to  
473 extension, and (2) ductile strain components of extensional faults, which are commonly overlooked.  
474 Similar missing extensional components are expected in this MTC. Assuming normal fault populations  
475 follow fractal size distributions, it is possible to estimate the missing extensional strain using the heave  
476 and number of observable faults (Marrett & Allmendinger 1992; Knott et al. 1996). Using this  
477 relationship, we can estimate extension of sub-seismic extensional faults ( $h_{sf}$ ) by measuring heaves on  
478 the observable faults ( $h_{if}$ ), where  $N$  = number of faults and  $C$  = characterises the relative numbers of  
479 sub-seismic to observable faults (Marrett & Allmendinger 1992).

480

$$481 \quad h_{sf} = h_{if} \frac{C}{1-C} (N + 1) \left( \frac{N}{N+1} \right)^{1/N} \quad (2)$$

482

483 The above equation is very sensitive to the linear relationship between  $N$  and displacement, and hence  
484 variations in exponent  $C$ . When using 3D-seismic reflection data, Gauthier & Lake (1993) found that,  
485 in most cases,  $C = \sim 1$ , ranging from 0.8-1.5. For Section 1, we estimate between 17-40% additional  
486 extension from sub-seismic faulting, assuming  $C = 0.9-1.1$ ,  $h_{if} = 1.88$  km and  $N = 13$ . This value is in  
487 line with other estimates of missing extensional strain and eloquently demonstrates the limitations of  
488 palinspastic restoration.

489 With the recognition of missing strain components, we are inevitably underestimating shortening and  
490 extension. This inference may suggest that the MTC interpretation is less balanced than Table 1

491 suggests. However, we could extrapolate these missing components (compression 30%+, extension c.  
492 17-40) to assume that if, on a seismic-scale, the MTC broadly balances we may suggest that on a sub-  
493 seismic scale the system also balances. Further, detailed fieldwork and modelling (physical and  
494 numerical) may be required to validate sub-seismic balancing. However, balancing of extensional and  
495 compressional domains seems a reasonable hypothesis to propose.

496

#### 497 *Overprinting, polyphase deformation and cell flow models*

498 Classic single-cell dislocation models describe the idealised case of a single MTC sheet, referred to as  
499 a “cell”, propagating downslope, with up-dip extension balanced by down-dip contraction (Lewis 1971;  
500 Farrell 1984). The model suggests an initial point of failure along a weak detachment layer where  
501 compression develops downslope and extension develops upslope of this point (Farrell 1984). This  
502 concept is useful for gaining a first-order understanding of MTCs gross-structure but, as many field  
503 studies have shown, is oversimplified (e.g. Martinsen & Bakken 1990).

504 Our MTC displays many of the features proposed by single-celled models such as (1) downslope thrust  
505 patterns, and (2) basinward fold-vergence. However, as Farrell (1984) notes in the original model, a  
506 component of “anti-dislocation” (i.e. propagation of strain through the MTC as it ceases translation)  
507 may cause overprinting of primary structures. The overprinting would come about due to the  
508 termination of shear failure on the basal shear surface occurring at either the head or toe of the MTC.  
509 Practically this would mean (1) if the toe ceased first then contractional strain would propagate upslope,  
510 or (2) if the head ceased first then extensional strain would propagate downslope, until the full mass of  
511 the MTC has come to rest. This leads to the formation of additional structures such as shear fractures,  
512 dilatational (mode 1) fractures, and thrusts that overprint the originally formed structures (e.g. Alsop &  
513 Marco 2011). Explanations for this added structural heterogeneity have focused on the theory of multi-  
514 cell models, where a large, first-order MTC cell is composed of many transient secondary-order flow  
515 cells that locally interact and overprint related features (Alsop & Marco 2014). Similarly, identification  
516 of polyphase deformation/accumulation of multiple event from seismic-field integrated studies (e.g.  
517 Ogata et al. 2014) shows added intricacy when compared to the single-celled model assumption.

518 We suggest towards the eastern part of the MTC, compressional overprinting fabrics may have been  
519 preserved within a predominately extensional domain, as the fold-thrust system is seen much further  
520 updip. In addition, the longitudinal and sub-orthogonal shear zones represent velocity variations and  
521 potentially cell boundaries within a larger first-order MTC. Therefore, although extensional-  
522 translational-compressional sequences are often most appropriate when assessing MTC at a seismic  
523 scale, strain-overprinting should be considered together with structural restoration results. One potential  
524 way to account for this complexity would be to treat each cell as a separate structural restoration case.  
525 Identifying any strain discrepancies between and within cells could then be compared to the overall  
526 single-celled model.

527

## 528 **7. CONCLUSIONS**

529 (1) A structurally-complex Neogene MTC has been identified on the lower slope within the deep-water  
530 passive margin sequence, offshore Uruguay. A shear coupling type emplacement model is proposed,  
531 where an overriding debris flow(s) produced increased loading and localisation of shear stress on a  
532 mechanically weak zone, which subsequently underwent shear failure.

533 (2) 3D seismic-reflection data, including several seismic attributes, enabled kinematic indicators to be  
534 determined from the following features: rafted-blocks, lateral margins and fold-thrust systems. In  
535 addition, two previously undocumented seismic kinematic indicators were identified: (1) sub-

536 orthogonal shear zones, and (2) the formation of fold-thrust systems within the kinematic boundary  
537 zone beneath rafted-blocks. Characterisation of the MTC enabled a paleo-slope and transport direction  
538 to be identified and the correct orientation of structural restoration models to be constrained.

539 (3) This is the first study to undertake structural restoration, including quantification of intra-MTC  
540 strain, within a single, completely preserved MTC. The results reveal that, on a seismic-scale, the MTC  
541 approximately balances, with 13-16% extension and 17-18% (c 25% without the frontally emergent  
542 zone) compression. A depth-dependant layer-parallel shortening is identified within the compressional  
543 domain that is consistent with other fold-thrust system models. One major uncertainty of the restoration  
544 models is the missing components of sub-seismic/penetrative strain that are likely contributing  
545 significantly to shortening and extension.

546 (4) Using conventional seismic-analysis and classification the MTC could be split into a broadly tri-  
547 partite strain distribution with extensional, translational and compressional domains. However, after  
548 undertaking detailed seismic extractions and appreciating the limited nature of the translational domain,  
549 it is concluded that a bi-partite strain distribution, with an appreciation of strain overprinting processes,  
550 may be a more accurate way to describe many MTCs.

551 (5) The assumption of a structurally balanced MTC is a simple high-level concept. However, proving  
552 this based on natural examples is difficult due to a combination of the complex and often polyphase  
553 deformation history, and dataset limitations.

554

555

556

557

558

559 *Acknowledgments*

560 *Thank you to ANCAP and Shell for providing the dataset and allowing publication of the paper. Thank*  
561 *you to Schlumberger, ffa Geoteric and Midland Valley Exploration for software donations. Thank you*  
562 *to Alexander Coleman for persisting to teach me 2D Move.*

563

564 **REFERENCES**

565 Alsop, G. & Holdsworth, R. 2007. Flow perturbation folding in shear zones. *Geological Society,*  
566 *London, Special Publications, 272*, 75-101.

567

568 Alsop, G. & Marco, S. 2011. Soft-sediment deformation within seismogenic slumps of the Dead Sea  
569 Basin. *Journal of Structural Geology, 33*, 433-457.

570

571 Alsop, G.I. & Marco, S. 2014. Fold and fabric relationships in temporally and spatially evolving  
572 slump systems: A multi-cell flow model. *Journal of Structural Geology, 63*, 27-49.

573

574 Alsop, G.I., Weinberger, R. & Marco, S. 2018. Distinguishing thrust sequences in gravity-driven fold  
575 and thrust belts. *Journal of Structural Geology*.

576

577 Alves, T.M. 2015. Submarine slide blocks and associated soft-sediment deformation in deep-water  
578 basins: a review. *Marine and Petroleum Geology, 67*, 262-285.

579

580 Alves, T.M. & Lourenço, S.D. 2010. Geomorphologic features related to gravitational collapse:  
581 Submarine landsliding to lateral spreading on a late Miocene–Quaternary slope (SE Crete, eastern  
582 Mediterranean). *Geomorphology, 123*, 13-33.

583

584 Armandita, C., Morley, C.K. & Rowell, P. 2015. Origin, structural geometry, and development of a  
585 giant coherent slide: The South Makassar Strait mass transport complex. *Geosphere, 11*, 376-403.

586

587 Armitage, D.A. & Stright, L. 2010. Modeling and interpreting the seismic-reflection expression of  
588 sandstone in an ancient mass-transport deposit dominated deep-water slope environment. *Marine and*  
589 *Petroleum Geology, 27*, 1-12.

590

591 Bull, S., Cartwright, J. & Huse, M. 2009. A review of kinematic indicators from mass-transport  
592 complexes using 3D seismic data. *Marine and Petroleum Geology, 26*, 1132-1151.

593

594 Burberry, C.M. 2015. Spatial and temporal variation in penetrative strain during compression:  
595 Insights from analog models. *Lithosphere, 7*, 611-624.

596

597 Butler, R. & Paton, D. 2010. Evaluating lateral compaction in deepwater fold and thrust belts: How  
598 much are we missing from “nature’s sandbox”. *GSA Today, 20*, 4-10.

599

600 Butler, R.W., Eggenhuisen, J.T., Haughton, P. & McCaffrey, W.D. 2016. Interpreting syndepositional  
601 sediment remobilization and deformation beneath submarine gravity flows; a kinematic boundary  
602 layer approach. *Journal of the Geological Society, 173*, 46-58.

- 603  
604 Clare, M.A., Vardy, M.E., Cartigny, M.J., Talling, P.J., Himsworth, M.D., Dix, J.K., Harris, J.M.,  
605 Whitehouse, R.J., et al. 2017. Direct monitoring of active geohazards: emerging geophysical tools for  
606 deep-water assessments. *Near Surface Geophysics*, **15**, 427-444.
- 607  
608 Conti, B., de Jesus Perinotto, J.A., Veroslavsky, G., Castillo, M.G., de Santa Ana, H., Soto, M. &  
609 Morales, E. 2017. Speculative petroleum systems of the southern Pelotas Basin, offshore Uruguay.  
610 *Marine and Petroleum Geology*, **83**, 1-25.
- 611  
612 Craddock, J.P. & van der Pluijm, B.A. 1989. Late Paleozoic deformation of the cratonic carbonate  
613 cover of eastern North America. *Geology*, **17**, 416-419.
- 614  
615 Dahlstrom, C. 1969. Balanced cross sections. *Canadian Journal of Earth Sciences*, **6**, 743-757.
- 616  
617 Dalton, T., Paton, D., Oldfield, S., Needham, D. & Wood, A. 2017. The importance of missing strain  
618 in Deep Water Fold and Thrust Belts. *Marine and Petroleum Geology*, **82**, 163-177.
- 619  
620 Debacker, T.N., Dumon, M. & Matthys, A. 2009. Interpreting fold and fault geometries from within  
621 the lateral to oblique parts of slumps: a case study from the Anglo-Brabant Deformation Belt  
622 (Belgium). *Journal of Structural Geology*, **31**, 1525-1539.
- 623  
624 Dott, R. 1963. Dynamics of subaqueous gravity depositional processes. *AAPG Bulletin*, **47**, 104-128.
- 625  
626 Farrell, S. 1984. A dislocation model applied to slump structures, Ainsa Basin, South Central  
627 Pyrenees. *Journal of Structural Geology*, **6**, 727-736.
- 628  
629 Fleming, R.W. & Johnson, A.M. 1989. Structures associated with strike-slip faults that bound  
630 landslide elements. *Engineering Geology*, **27**, 39-114.
- 631  
632 Fossen, H. 2016. *Structural geology*. Cambridge University Press.
- 633  
634 Franke, D., Neben, S., Ladage, S., Schreckenberger, B. & Hinz, K. 2007. Margin segmentation and  
635 volcano-tectonic architecture along the volcanic margin off Argentina/Uruguay, South Atlantic.  
636 *Marine Geology*, **244**, 46-67.
- 637  
638 Frey-Martínez, J., Cartwright, J. & James, D. 2006. Frontally confined versus frontally emergent  
639 submarine landslides: a 3D seismic characterisation. *Marine and Petroleum Geology*, **23**, 585-604.
- 640  
641 Gamboa, D. & Alves, T.M. 2015. Three-dimensional fault meshes and multi-layer shear in mass-  
642 transport blocks: Implications for fluid flow on continental margins. *Tectonophysics*, **647**, 21-32.
- 643  
644 Gamboa, D. & Alves, T.M. 2016. Bi-modal deformation styles in confined mass-transport deposits:  
645 Examples from a salt minibasin in SE Brazil. *Marine Geology*, **379**, 176-193.
- 646  
647 Gauthier, B. & Lake, S. 1993. Probabilistic modeling of faults below the limit of seismic resolution in  
648 Pelican Field, North Sea, offshore United Kingdom. *AAPG Bulletin*, **77**, 761-777.

- 649  
650 Gee, M., Gawthorpe, R. & Friedmann, J. 2005. Giant striations at the base of a submarine landslide.  
651 *Marine Geology*, **214**, 287-294.
- 652  
653 Gee, M., Gawthorpe, R. & Friedmann, S. 2006. Triggering and evolution of a giant submarine  
654 landslide, offshore Angola, revealed by 3D seismic stratigraphy and geomorphology. *Journal of*  
655 *Sedimentary Research*, **76**, 9-19.
- 656  
657 Groshong, R.H., Withjack, M.O., Schlische, R.W. & Hidayah, T.N. 2012. Bed length does not remain  
658 constant during deformation: Recognition and why it matters. *Journal of Structural Geology*, **41**, 86-  
659 97.
- 660  
661 Henry, P., Jouniaux, L., Screaton, E.J., Hunze, S. & Saffer, D.M. 2003. Anisotropy of electrical  
662 conductivity record of initial strain at the toe of the Nankai accretionary wedge. *Journal of*  
663 *Geophysical Research: Solid Earth*, **108**.
- 664  
665 Hodgson, D., Brooks, H., Ortiz-Karpf, A., Sychala, Y., Lee, D. & Jackson, C.-L. 2017. The  
666 entrainment and abrasion of megaclasts during submarine landsliding and their impact on flow  
667 behaviour. *Geological Society Special Publications*.
- 668  
669 Hossack, J.R. 1979. The use of balanced cross-sections in the calculation of orogenic contraction: A  
670 review. *Journal of the Geological Society*, **136**, 705-711.
- 671  
672 Hudec, M.R. & Jackson, M.P. 2004. Regional restoration across the Kwanza Basin, Angola: Salt  
673 tectonics triggered by repeated uplift of a metastable passive margin. *AAPG Bulletin*, **88**, 971-990.
- 674  
675 Jackson, C.A. 2011. Three-dimensional seismic analysis of megaclast deformation within a mass  
676 transport deposit; implications for debris flow kinematics. *Geology*, **39**, 203-206.
- 677  
678 Kautz, S.A. & Sclater, J.G. 1988. Internal deformation in clay models of extension by block faulting.  
679 *Tectonics*, **7**, 823-832.
- 680  
681 Knott, S.D., Beach, A., Brockbank, P.J., Brown, J.L., McCallum, J.E. & Welbon, A.I. 1996. Spatial  
682 and mechanical controls on normal fault populations. *Journal of Structural Geology*, **18**, 359-372.
- 683  
684 Koyi, H. 1995. Mode of internal deformation in sand wedges. *Journal of Structural Geology*, **17**,  
685 293297-295300.
- 686  
687 Koyi, H.A., Sans, M., Teixell, A., Cotton, J. & Zeyen, H. 2004. The significance of penetrative strain  
688 in the restoration of shortened layers—Insights from sand models and the Spanish Pyrenees.
- 689  
690 Krastel, S., Wefer, G., Hanebuth, T.J., Antobreh, A.A., Freudenthal, T., Preu, B., Schwenk, T.,  
691 Strasser, M., et al. 2011. Sediment dynamics and geohazards off Uruguay and the de la Plata River  
692 region (northern Argentina and Uruguay). *Geo-Marine Letters*, **31**, 271-283.
- 693

- 694 Lamarche, G., Joanne, C. & Collot, J.Y. 2008. Successive, large mass-transport deposits in the south  
695 Kermadec fore-arc basin, New Zealand: The Matakaoa Submarine Instability Complex.  
696 *Geochemistry, Geophysics, Geosystems*, **9**.
- 697
- 698 Lewis, K. 1971. Slumping on a continental slope inclined at 1–4. *Sedimentology*, **16**, 97-110.
- 699
- 700 Lingrey, S. & Vidal-Royo, O. 2015. Evaluating the quality of bed length and area balance in 2D  
701 structural restorations. *Interpretation*, **3**, SAA133-SAA160.
- 702
- 703 Marrett, R. & Allmendinger, R.W. 1992. Amount of extension on "small" faults: An example from  
704 the Viking graben. *Geology*, **20**, 47-50.
- 705
- 706 Martinsen, O. 1994. Mass movements *The geological deformation of sediments*. Springer, 127-165.
- 707
- 708 Martinsen, O.J. & Bakken, B. 1990. Extensional and compressional zones in slumps and slides in the  
709 Namurian of County Clare, Ireland. *Journal of the Geological Society*, **147**, 153-164.
- 710
- 711 Masson, D., Huggett, Q. & Brunnsden, D. 1993. The surface texture of the Saharan debris flow deposit  
712 and some speculations on submarine debris flow processes. *Sedimentology*, **40**, 583-598.
- 713
- 714 Meckel, L. 2011. Reservoir characteristics and classification of sand-prone submarine mass-transport  
715 deposits. *SEPM Special Publication*, **96**, 432-452.
- 716
- 717 Merle, O. 1989. Strain models within spreading nappes. *Tectonophysics*, **165**, 57-71.
- 718
- 719 Moore, Z.T. & Sawyer, D.E. 2016. Assessing post-failure mobility of submarine landslides from  
720 seismic geomorphology and physical properties of mass transport deposits: An example from seaward  
721 of the Kumano Basin, Nankai Trough, offshore Japan. *Marine Geology*, **374**, 73-84.
- 722
- 723 Morales, E., Chang, H.K., Soto, M., Corrêa, F.S., Veroslavsky, G., de Santa Ana, H., Conti, B. &  
724 Daners, G. 2017. Tectonic and stratigraphic evolution of the Punta del Este and Pelotas basins  
725 (offshore Uruguay). *Petroleum Geoscience*, petgeo2016-2059.
- 726
- 727 Moscardelli, L. & Wood, L. 2015. Morphometry of mass-transport deposits as a predictive tool.  
728 *Geological Society of America Bulletin*, B31221. 31221.
- 729
- 730 Moscardelli, L., Wood, L. & Mann, P. 2006. Mass-transport complexes and associated processes in  
731 the offshore area of Trinidad and Venezuela. *AAPG Bulletin*, **90**, 1059-1088.
- 732
- 733 Nardin, T.R. 1979. A review of mass movement processes sediment and acoustic characteristics, and  
734 contrasts in slope and base-of-slope systems versus canyon-fan-basin floor systems.
- 735
- 736 Nemec, W. 1990. Aspects of sediment movement on steep delta slopes. *Coarse-grained deltas*, **10**,  
737 29-73.
- 738

- 739 Nürnberg, D. & Müller, R.D. 1991. The tectonic evolution of the South Atlantic from Late Jurassic to  
740 present. *Tectonophysics*, **191**, 27-53.
- 741  
742 Ogata, K., Mountjoy, J., Pini, G.A., Festa, A. & Tinterri, R. 2014. Shear zone liquefaction in mass  
743 transport deposit emplacement: A multi-scale integration of seismic reflection and outcrop data.  
744 *Marine Geology*, **356**, 50-64.
- 745  
746 Ortiz-Karppf, A., Hodgson, D.M., Jackson, C.A.L. & McCaffrey, W.D. 2016. Mass-transport  
747 complexes as markers of deep-water fold-and-thrust belt evolution: insights from the southern  
748 Magdalena fan, offshore Colombia. *Basin Research*, n/a-n/a, <http://doi.org/10.1111/bre.12208>.
- 749  
750 Partyka, G., Gridley, J. & Lopez, J. 1999. Interpretational applications of spectral decomposition in  
751 reservoir characterization. *The Leading Edge*, **18**, 353-360.
- 752  
753 Pickering, K.T. & Corregidor, J. 2005. Mass-transport complexes (MTCs) and tectonic control on  
754 basin-floor submarine fans, middle Eocene, south Spanish Pyrenees. *Journal of Sedimentary  
755 Research*, **75**, 761-783.
- 756  
757 Posamentier, H.W. & Kolla, V. 2003. Seismic geomorphology and stratigraphy of depositional  
758 elements in deep-water settings. *Journal of Sedimentary Research*, **73**, 367-388.
- 759  
760 Posamentier, H.W. & Martinsen, O.J. 2011. The character and genesis of submarine mass-transport  
761 deposits: insights from outcrop and 3D seismic data. *Mass-transport deposits in deepwater settings:  
762 Society for Sedimentary Geology (SEPM) Special Publication 96*, 7-38.
- 763  
764 Prior, D.B., Bornhold, B.D. & Johns, M. 1984. Depositional characteristics of a submarine debris  
765 flow. *The Journal of Geology*, **92**, 707-727.
- 766  
767 Rabinowitz, P.D. & LaBrecque, J. 1979. The Mesozoic South Atlantic Ocean and evolution of its  
768 continental margins. *Journal of Geophysical Research: Solid Earth*, **84**, 5973-6002.
- 769  
770 Randen, T. 1998. Automated Stratigraphic and Fault Interpretation. PCT Patent Application No  
771 PCT/IB99/01040.
- 772  
773 Randen, T., Pedersen, S.I. & Sønneland, L. 2001. Automatic extraction of fault surfaces from three-  
774 dimensional seismic data *SEG Technical Program Expanded Abstracts 2001*. Society of Exploration  
775 Geophysicists, 551-554.
- 776  
777 Rowan, M.G., Peel, F.J. & Vendeville, B.C. 2004. Gravity-driven fold belts on passive margins.
- 778  
779 Schlische, R.W., Groshong, R.H., Withjack, M.O. & Hidayah, T.N. 2014. Quantifying the geometry,  
780 displacements, and subresolution deformation in thrust-ramp anticlines with growth and erosion:  
781 From models to seismic-reflection profile. *Journal of Structural Geology*, **69**, 304-319.
- 782

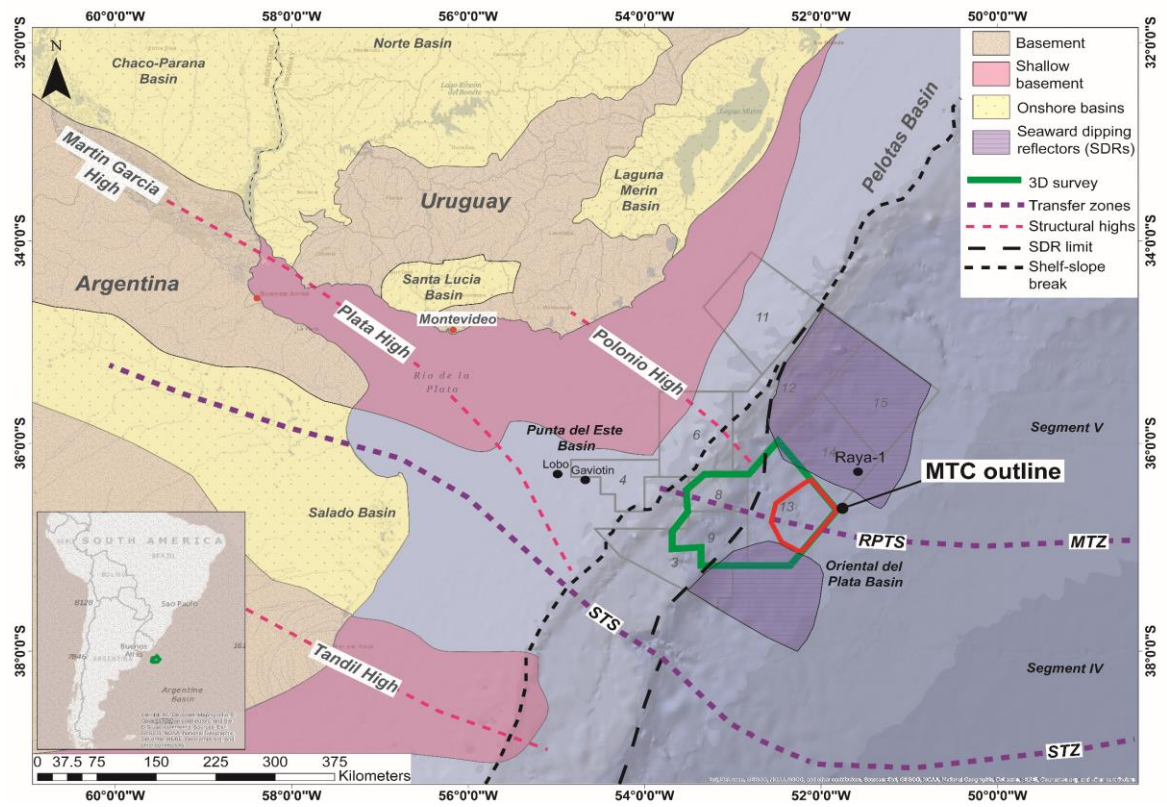
- 783 Schnellmann, M., Anselmetti, F.S., Giardini, D. & McKENZIE, J.A. 2005. Mass movement-induced  
784 fold-and-thrust belt structures in unconsolidated sediments in Lake Lucerne (Switzerland).  
785 *Sedimentology*, **52**, 271-289.
- 786  
787 Sclater, J.G. & Christie, P.A. 1980. Continental stretching: An explanation of the post-Mid-  
788 Cretaceous subsidence of the central North Sea Basin. *Journal of Geophysical Research: Solid Earth*,  
789 **85**, 3711-3739.
- 790  
791 Sharman, G.R., Graham, S.A., Masalimova, L.U., Shumaker, L.E. & King, P.R. 2015. Spatial patterns  
792 of deformation and paleoslope estimation within the marginal and central portions of a basin-floor  
793 mass-transport deposit, Taranaki Basin, New Zealand. *Geosphere*, **11**, 266-306.
- 794  
795 Sobiesiak, M.S., Alsop, G.I., Kneller, B. & Milana, J.P. 2017. Sub-seismic scale folding and thrusting  
796 within an exposed mass transport deposit: A case study from NW Argentina. *Journal of Structural*  
797 *Geology*, **96**, 176-191.
- 798  
799 Soto, M., Morales, E., Veroslavsky, G., de Santa Ana, H., Ucha, N. & Rodríguez, P. 2011. The  
800 continental margin of Uruguay: Crustal architecture and segmentation. *Marine and Petroleum*  
801 *Geology*, **28**, 1676-1689.
- 802  
803 Strachan, L. & Alsop, G.I. 2006. Slump folds as estimators of palaeoslope: a case study from the  
804 Fisherstreet Slump of County Clare, Ireland. *Basin Research*, **18**, 451-470.
- 805  
806 Van Bommel, P.P. & Pepper, R.E. 2000. Seismic signal processing method and apparatus for  
807 generating a cube of variance values. Google Patents.
- 808  
809 Van der Merwe, W., Hodgson, D. & Flint, S. 2009. Widespread syn-sedimentary deformation on a  
810 muddy deep-water basin-floor: the Vischkuil Formation (Permian), Karoo Basin, South Africa. *Basin*  
811 *Research*, **21**, 389-406.
- 812  
813 Van Der Merwe, W.C., Hodgson, D.M. & Flint, S.S. 2011. Origin and terminal architecture of a  
814 submarine slide: a case study from the Permian Vischkuil Formation, Karoo Basin, South Africa.  
815 *Sedimentology*, **58**, 2012-2038.
- 816  
817 Varnes, D.J. 1978. Slope movement types and processes. *Special report*, **176**, 11-33.
- 818  
819 Walsh, J., Watterson, J., Childs, C. & Nicol, A. 1996. Ductile strain effects in the analysis of seismic  
820 interpretations of normal fault systems. *Geological Society, London, Special Publications*, **99**, 27-40.
- 821  
822 Wang, F., Dai, Z. & Zhang, S. 2017. Experimental study on the motion behavior and mechanism of  
823 submarine landslides. *Bulletin of Engineering Geology and the Environment*, 1-10.
- 824  
825 Watt, S., Talling, P., Vardy, M., Masson, D., Henstock, T., Hühnerbach, V., Minshull, T., Urlaub, M.,  
826 et al. 2012. Widespread and progressive seafloor-sediment failure following volcanic debris  
827 avalanche emplacement: Landslide dynamics and timing offshore Montserrat, Lesser Antilles. *Marine*  
828 *Geology*, **323**, 69-94.

829  
830  
831  
832  
833  
834  
835  
836  
837  
838  
839  
840  
841  
842  
843  
844  
845  
846  
847  
848  
849  
850  
851

Weimer, P. 1990. Sequence Stratigraphy, Facies Geometries, and Depositional History of the Mississippi Fan, Gulf of Mexico (1). *AAPG Bulletin*, **74**, 425-453.

Weimer, P. & Shipp, C. 2004. Mass transport complex: musing on past uses and suggestions for future directions. *Offshore Technology Conference*. Offshore Technology Conference.

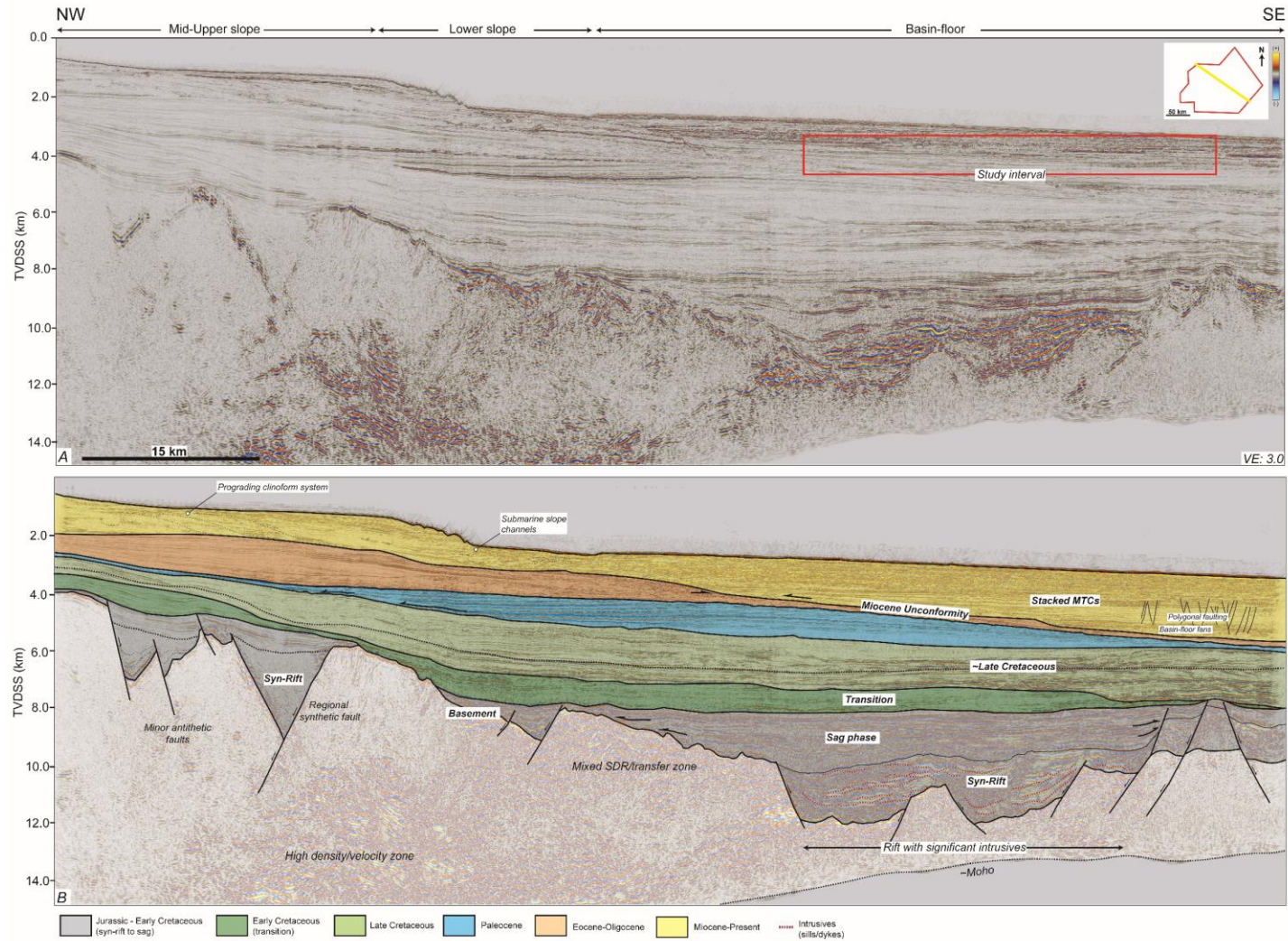
Zeng, H., Henry, S.C. & Riola, J.P. 1998. Stratal slicing, part II: Real 3-D seismic data. *Geophysics*, **63**, 514-522.



852

853 *Figure 1: Study area offshore Uruguay, onshore/offshore basins outlines and structural highs from ANCAP and Soto et al.*  
 854 *(2011), landward limit of seaward dipping reflectors from Franke et al. (2007), note current licence blocks and Lobo and*  
 855 *Gaviotin wells, dataset (green) and study area (red) outlines, Raya-1 location from spectrumgeo.*

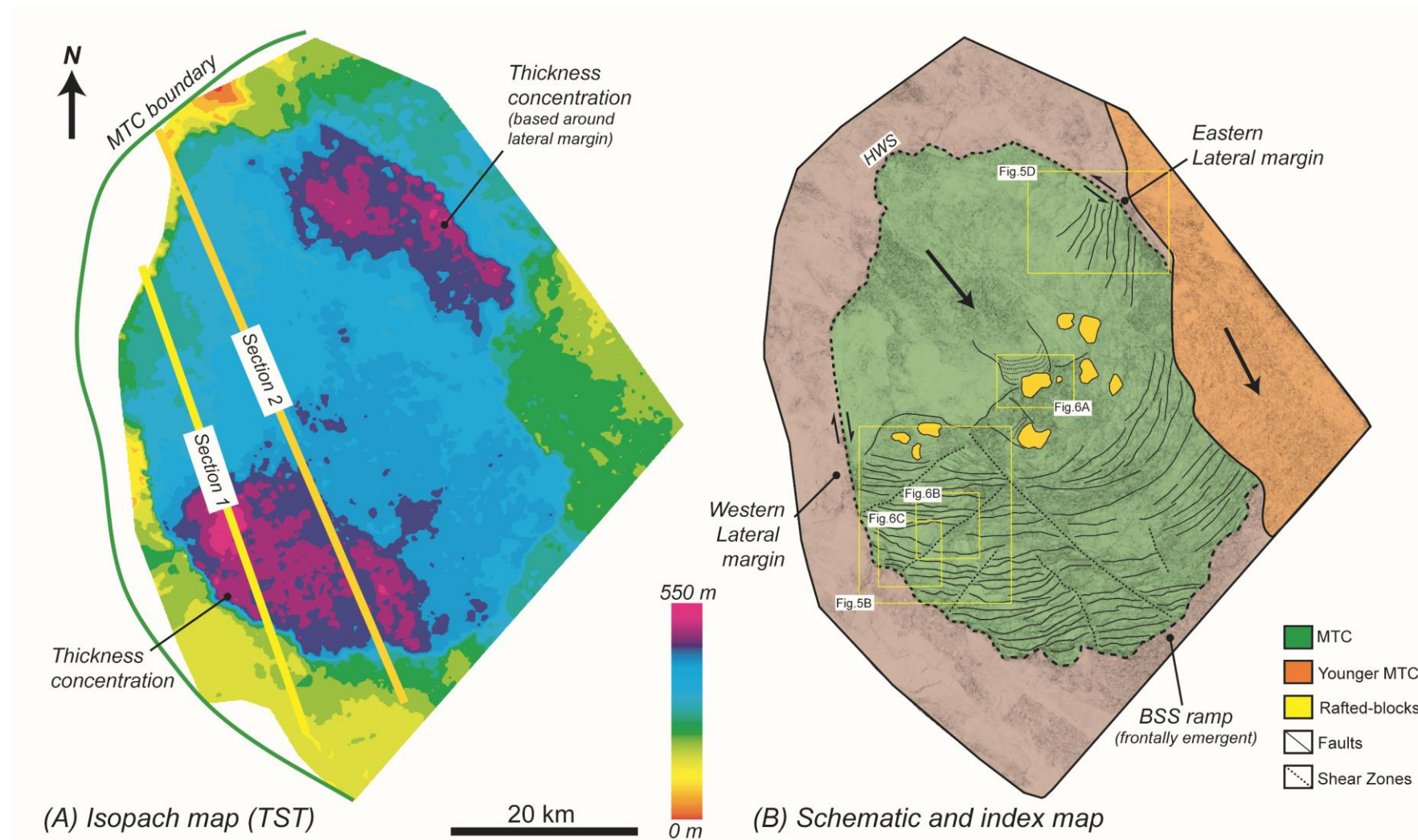
856



857

858 Figure 2: (A) Dip seismic section, (B) geosection, through the central Uruguay margin spanning the continental to transitional crust with significant volcanic components including SDRs, a  
 859 high density underplating zone and intrusives. Stratigraphic ages are estimated from Morales et al. (2017) and ANCAP. Note the study area, located down-dip from a large prograding  
 860 clinoform system.

861

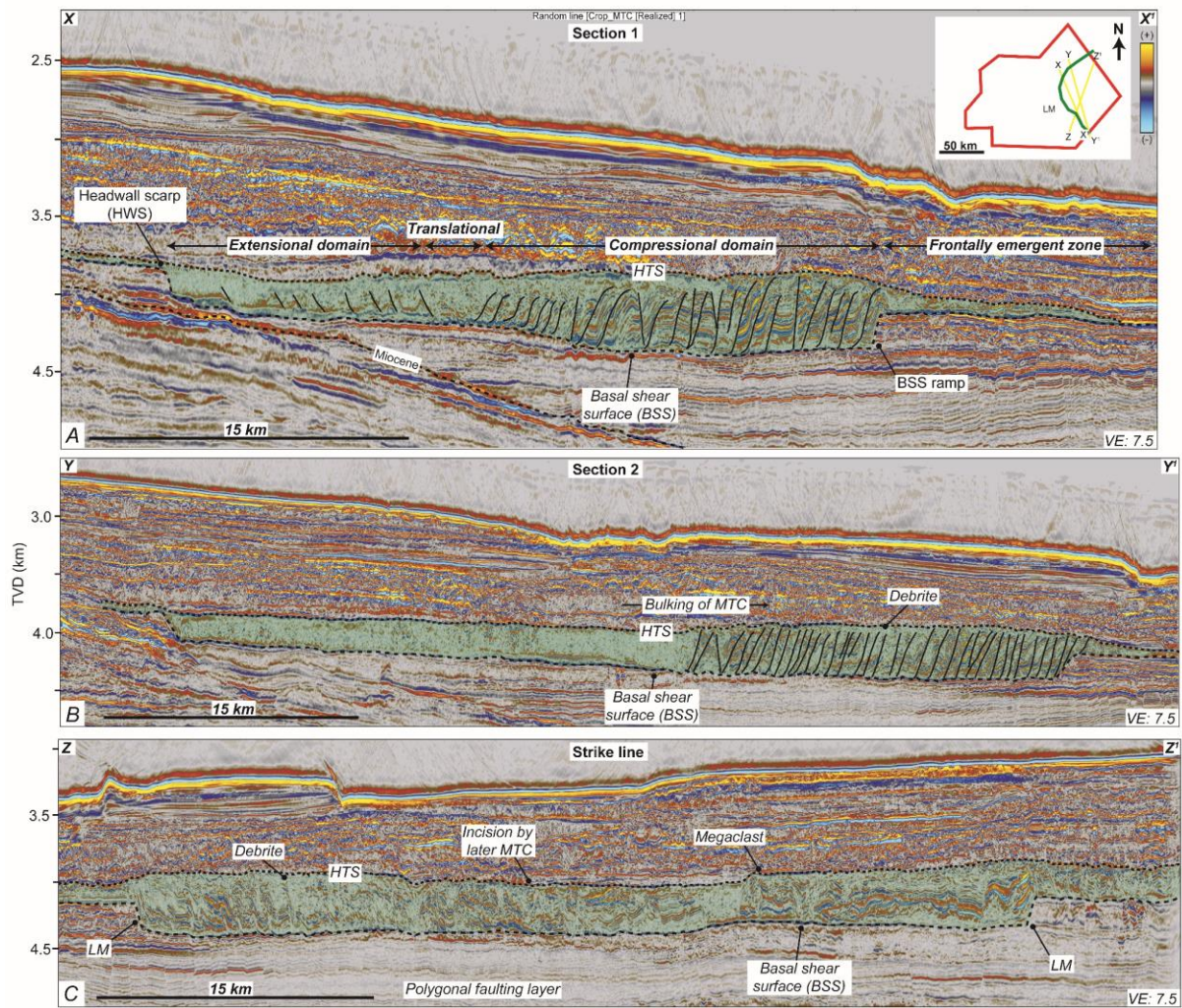


862

863

864

Figure 3: (A) Isopach map displayed in true stratigraphic thickness, between the basal shear surface (BSS) and top surface. Note Sections 1 and 2 which are the dip sections chosen for structural restoration, (B) Schematic and index map of main structural elements within the MTC and reference locations for later figures.



865

866

867

868

869

870

Figure 4. (A) Dip seismic Section 1, used for structural restoration, note the well-defined extensional and compressional domains (B) Dip seismic Section 2 used for structural restoration located more centrally within the MTC, note the overlying chaotic debris (C) Strike seismic section highlighting distinct lateral margins, megaclasts and incision of the top surface, HTS = hummocked top surface, LM = lateral margins. Amplitudes have been compressed to account for washout from very high amplitude gas charged sediment above the study interval

871

872

873

874

875

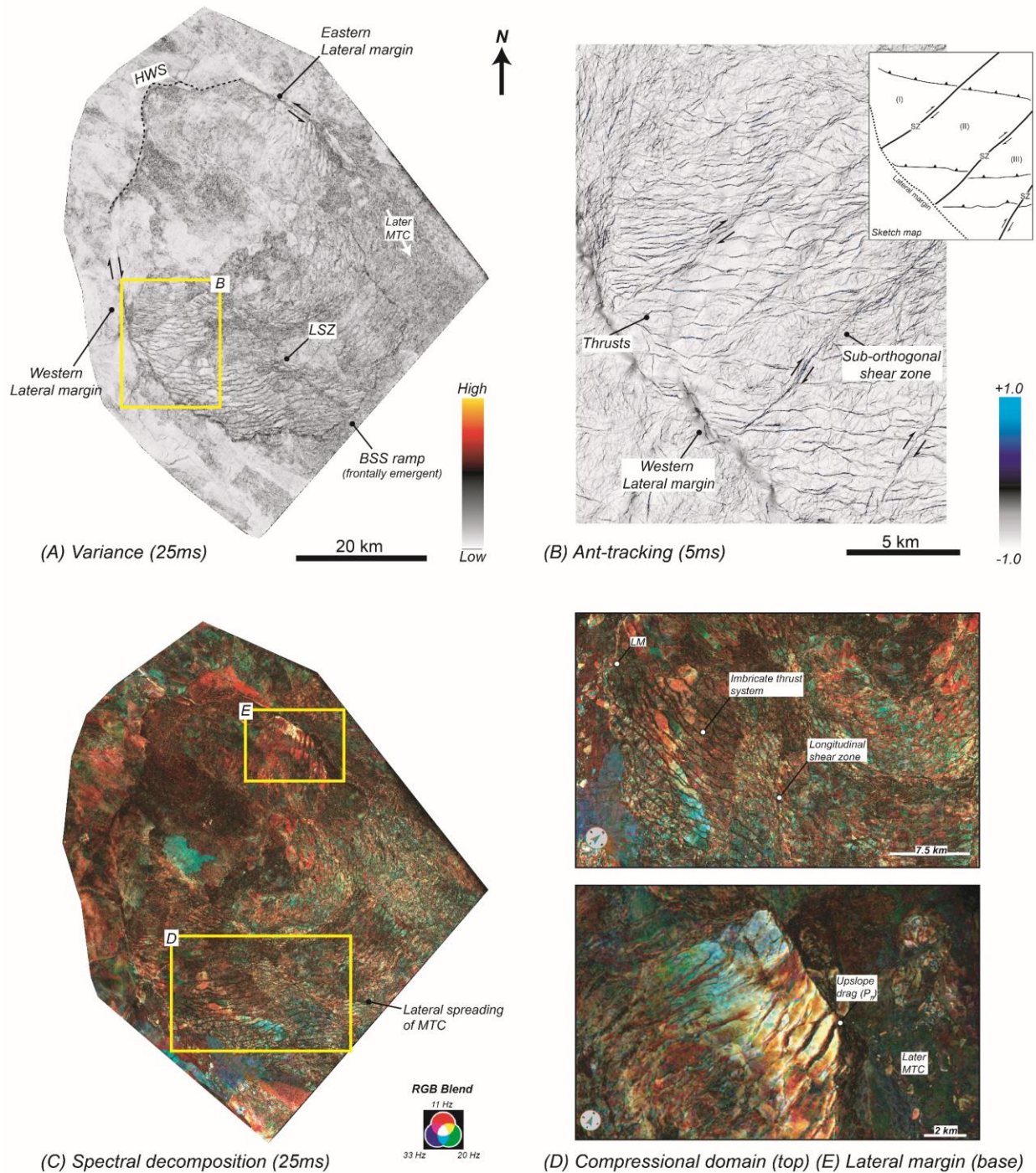
876

877

878

879

880



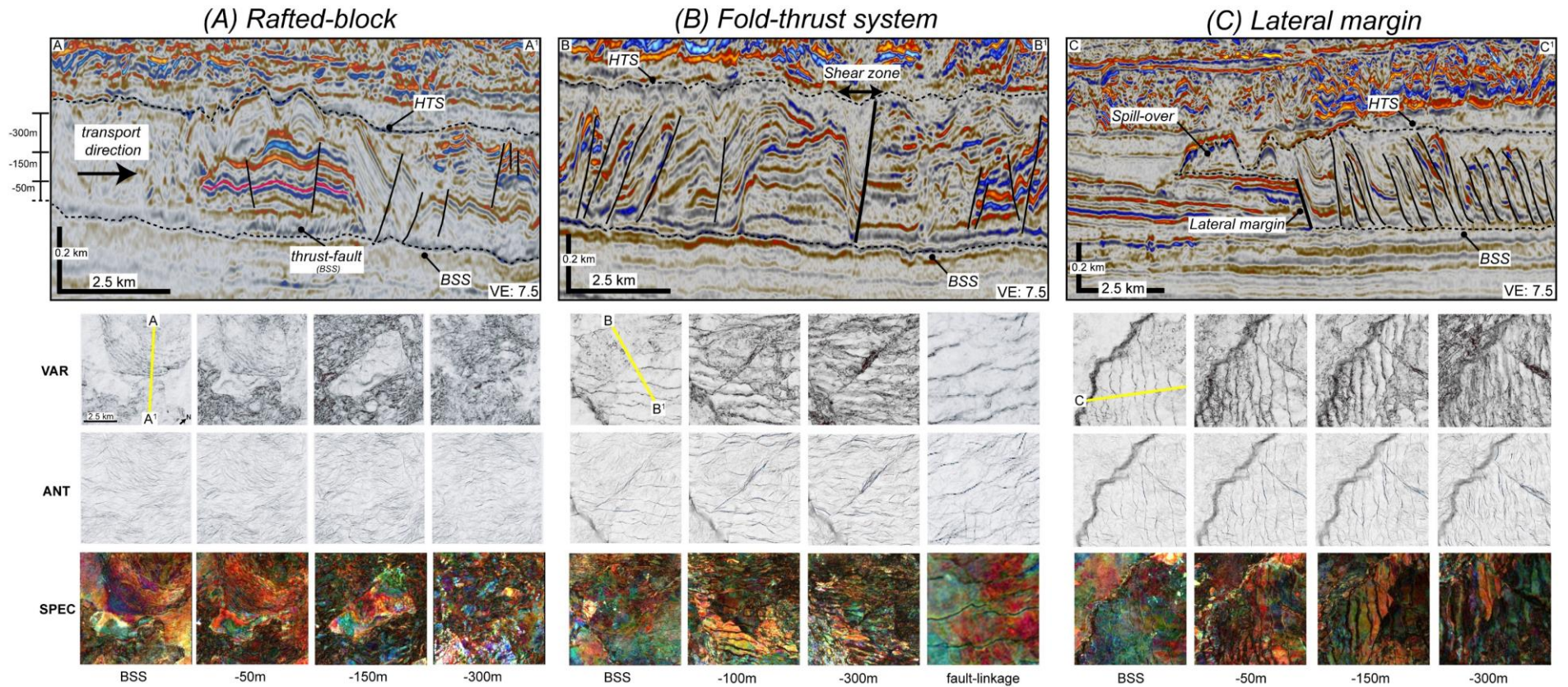
881

882 Figure 5: (A) Variance extraction from the basal shear surface over a 25ms window, delineating the lateral margins,  
 883 frontally emergent ramp and longitudinal shear zone (LSZ), (B) Ant-track extraction from the basal shear surface over a  
 884 5ms, imaging the interaction between the western lateral margin and sub-orthogonal shear zones, (C) Spectral  
 885 decomposition extraction from the basal shear surface over a 25ms window, note locations of D and E, (D) Compressional  
 886 domain imaging imbricate thrust systems, (E) Eastern lateral margin imaging upslope drag and erosion by a younger MTC.

887

888

889

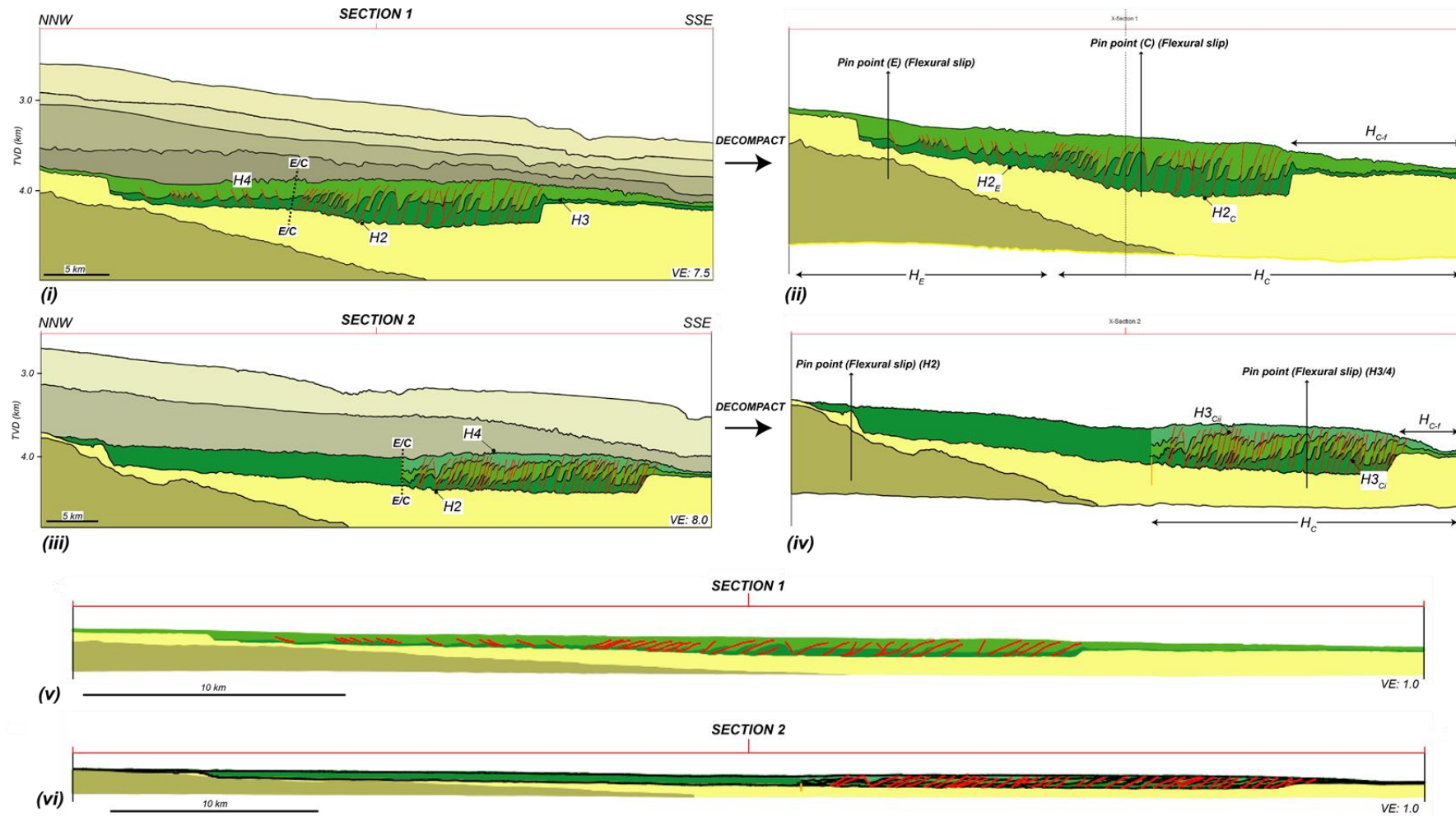


890

891 *Figure 6: Iso-proportional variance (VAR), ant-track (ANT) and spectral decomposition (SPEC) extractions between the BSS and top surface (HTS), (A) Seismic dip line displaying rafted-*  
 892 *block, BSS thrust faults and intra-block normal faults, BSS to -300 above demonstrating the through going nature of the fault systems, (B) Seismic line through MTC thrust-fault system and*  
 893 *orthogonal shear zone seen to detach onto the BSS, fault linkage (relay ramps) imaged between thrust faults, (C) Seismic line highlighting the abrupt western lateral margin, note the irregular*  
 894 *nature of the thrust as they interact with the lateral margin*

895

896



897

898

899 Figure 7: Decompressed structural restoration models, (i) section 1 present day section, (ii) section 1 decompacted section, (iii) section 2 present day section, (iv) section 2 decompacted section.  
 900 Section 1 sits near the western lateral margin of the MTC, section 2 crosses centrally through the main MTC body, note pin points used for flexural slip calculations, (v/vi) Vertically  
 901 exaggeration 1.0.

902 Table 1: Results of structural restoration, (+) extension, (-) compression

<i>Restoration Method</i>	<i>Horizon</i>	<i>Present-length (m)</i>	<i>Restored-length (m)</i>	<i>Missing length (m)</i>	<i>Strain (e)</i>
<b>Section 1</b>					
Line-length	H2	51600	52024	424	-0.8
	H3	46206	51827	5621	-10.8
	H4	51600	51708	108	-0.2
	H3 <sub>E</sub>	13900	12002	-1898	15.8
	H3 <sub>C</sub>	32345	39824	7480	-18.8
	H3 <sub>C-f</sub>	20585	27983	7398	-26.4
Simple/vertical shear (90 deg)	H2	51600	51602	2	0.0
	H3	46206	51058	4852	-9.5
	H4	51600	51598	-2	0.0
	H3 <sub>E</sub>	13900	12218	-1682	13.8
	H3 <sub>C</sub>	32345	39152	6808	-17.4
	H3 <sub>C-f</sub>	20585	27359	6774	-24.8
Flexural slip	H2	51600	52024	424	-0.8
	H3	46206	51826	5620	-10.8
	H4	51600	51708	108	-0.2
	H3 <sub>E</sub>	13900	12316	-1584	12.9
	H3 <sub>C</sub>	32345	39825	7481	-18.8
	H3 <sub>C-f</sub>	20585	27982	7397	-26.4
<b>Section 2</b>					
Line-length	H2	65000	65675	675	-1.0
	H4	63800	64404	604	-0.9
	H3 <sub>Ci</sub>	24058	32894	8836	-26.9
	H3 <sub>Cii</sub>	30028	35404	5376	-15.2
	H3 <sub>Cii-f</sub>	23963	29056	5093	-17.5
Simple shear (unfold 90 deg )	H2	65000	65028	28	0.0
	H4	63800	63836	36	-0.1
	H3 <sub>Ci</sub>	24058	31812	7754	-24.4
	H3 <sub>Cii</sub>	30028	34922	4894	-14.0
	H3 <sub>Cii-f</sub>	23963	28593	4630	-16.2
Flexural slip	H2	65000	65681	681	-1.0
	H4	63800	64460	660	-1.0
	H3 <sub>Ci</sub>	24058	32895	8837	-26.9
	H3 <sub>Cii</sub>	30028	35404	5376	-15.2
	H3 <sub>Cii-f</sub>	23963	29057	5094	-17.5

903

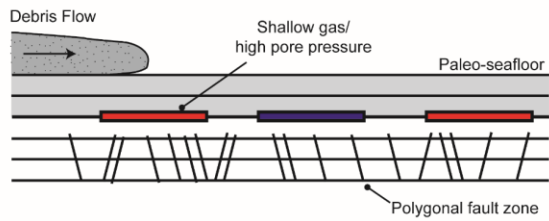
904

905

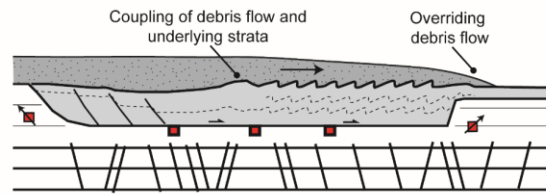
906

907

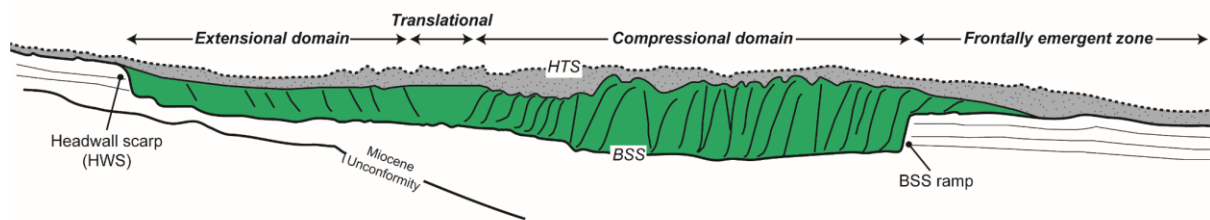
Stage 1: Initiation (shear strength  $\geq$  stress)



Stage 2: Shear coupling (shear strength  $<$  stress)



Stage 3: MTC



908

909

910

911

Figure 8: MTC emplacement model, stage 1 initiation through overriding debris flow producing localisation of shear stress on a mechanically weak likely shallow gas filled zone, stage 2 in situ failure of underlying sediments through shear coupling, stage 3 failure of underlying sediments has produced significant extensional and compressional domains.

912

913

914